www.sciencemag.org/cgi/content/full/314/5806/1731/DC1

Supporting Online Material for

Elemental Compositions of Comet 81P/Wild 2 Samples Collected by Stardust

George J. Flynn,* Pierre Bleuet, Janet Borg, John P. Bradley, Frank E. Brenker, Sean Brennan, John Bridges, Don E. Brownlee, Emma S. Bullock, Manfred Burghammer, Benton C. Clark, Zu Rong Dai, Charles P. Daghlian, Zahia Djouadi, Sirine Fakra, Tristan Ferroir, Christine Floss, Ian A. Franchi, Zack Gainsforth, Jean-Paul Gallien, Philippe Gillet, Patrick G. Grant, Giles A. Graham, Simon F. Green, Faustine Grossemy, Philipp R. Heck, Gregory F. Herzog, Peter Hoppe, Friedrich Hörz, Joachim Huth, Konstantin Ignatyev, Hope A. Ishii, Koen Janssens, David Joswiak, Anton T. Kearsley, Hicham Khodja, Antonio Lanzirotti, Jan Leitner, Laurence Lemelle, Hugues Leroux, Katharina Luening, Glenn J. MacPherson, Kuljeet K. Marhas, Matthew A. Marcus, Graciela Matrajt, Tomoki Nakamura, Keiko Nakamura-Messenger, Tsukasa Nakano, Matthew Newville, Dimitri A. Papanastassiou, Piero Pianetta, William Rao, Christian Riekel, Frans J. M. Rietmeijer, Detlef Rost, Craig S. Schwandt, Thomas H. See, Julie Sheffield-Parker, Alexandre Simionovici, Ilona Sitnitsky, Christopher J. Snead, Frank J. Stadermann, Thomas Stephan, Rhonda M. Stroud, Jean Susini, Yoshio Suzuki, Stephen R. Sutton, Susan Taylor, Nick Teslich, D. Troadec, Peter Tsou, Akira Tsuchiyama, Kentaro Uesugi, Bart Vekemans, Edward P. Vicenzi, Laszlo Vincze, Andrew J. Westphal, Penelope Wozniakiewicz, Ernst Zinner, Michael E. Zolensky

*To whom correspondence should be addressed. E-mail: george.flynn@plattsburgh.edu

Published 15 December 2006, *Science* **314**, 1731 (2006)

DOI: 10.1126/science.1136141

This PDF file includes:

Supporting Online Materials

Synchrotron X-Ray Microprobe Analysis

Synchrotron X-Ray Microprobes (SXRMs) employ tunable, high-intensity x-ray beams to excite x-ray fluorescence in a sample, and collect the x-ray spectrum allowing quantification of element abundances in the probe spot. The incident x-ray photon energy is high enough that it penetrates completely through an aerogel keystone, providing a relatively uniform excitation as a function of particle depth. The major limitation on element detection is the escape depth of the fluorescence x-rays, which limited these analyses to elements with an atomic number $\geq$ 16 (sulfur). SXRMs do not suffer from the relatively large Bremstrahlung background, which limits the sensitivity of electron beam analysis by the fluorescence technique. The high sensitivity of XRMs allows element detection down to tens of attograms in the analysis spot of some instruments with sufficiently long integration times. For the x-ray fluorescence mapping of aerogel keystones, the element distribution was determined by raster-scanning the area containing the track, and generating element abundance maps.

The 6-month time period of the Stardust preliminary examination, coupled with the instrument time required to analyze the small amount of material distributed along each track in the Stardust aerogel, required an international collaboration to analyze a sufficient amount of material from the Stardust collection to establish a meaningful mean composition. The measurements that produced the results in Table S1 were performed at 6 synchrotrons: the Stanford Synchrotron Radiation Laboratory (Stanford Linear Accelerator Center, Menlo Park, CA USA), the Advanced Light Source (Lawrence Berkeley National Laboratory, Berkeley, CA USA), the Advanced Photon Source (Argonne National Laboratory, Argonne, IL USA), theNational Synchrotron Light Source (Brookhaven National Laboratory, Upton, NY USA), the European Synchrotron Radiation Facility (Grenoble, France), and SPring-8 (Hyougo, Japan). The SXRMs at these synchrotrons, which differ in their analytical capabilities and analysis conditions, are described below.

Prior to the Stardust landing, Allende powder and powder from a microprobe standard hornblende, provided as an "unknown," were shot into aerogel cells. Tracks containing both materials were prepared as aerogel keystones, and provided to each group participating in the SXRM analysis of Stardust samples during the Preliminary Examination. The Allende samples were used to provide an indication of the elements each instrument can detect in a chondritic sample while the "unknown" was used to insure consistency in analyses among the laboratories. Even for a relatively strong material like Allende, a considerable amount of material was deposited along the entry track, so we anticipated that in order to determine the chemical compositions of the Wild 2 particles it would be necessary to integrate the chemical composition over the material along the entry track, rather than concentrating on the analysis of the terminal particles.

European Synchrotron Radiation Facility X-Ray Microprobes

The ESRF ID22 and ID21 beamlines, dedicated to high- and low-energy microspectroscopy respectively, were used for analyses of tracks in keystones. Initially, whole track analyses were done on ID22, at 13 keV incident energy, with either 2×2 or 2×4 micrometers resolution (for the very large maps) and $1x10^{11}$ photons/s in the beamspot. A 13-element Gresham Si(Li) detector, set in the horizontal plane at 90° to the beam direction, was used for the fluorescence detection and two PIN diodes were used to monitor the x-ray beam intensity before/after the sample. High resolution maps were taken of 20×20 square micrometer areas around the terminal particles, with 1 micrometer resolution and 1 sec/point acquisitions. The x-ray beam was monochromatized by a Si 111 flat double crystal Kohzu monochromator and focused by a remote controlled double bent Kirkpatrick-Baez (K-B) mirror device. For some keystones, XANES around the respective

K edges of Fe or S was performed, on the ID21, using a Si 111 monochromator. Fresnel zone plate lenses were used there to produce square beamspots of 1x1 micrometers for Fe-XANES and 0.3x0.3 micrometers S-XANES with about $1x10^9$ photons/s. A thin Kapton foil coupled to a Si PIN diode was used to monitor the incident beam intensity and a high resolution HpGe detector for fluorescence.

Spectra were acquired and processed as follows: All tracks (T) and terminal particles (TP) including corresponding aerogel areas surrounding the tracks were mapped with either 2x2 or 2x4 square micron beamspots. We used an 0.5 to 1 second real time setting for acquisition of fluorescence spectra while insuring that the pile-up effects never produced saturation higher than 15%, corrected by the XIA digital signal processor used. The Fe signal was used to establish which parts of the map contained fluorescence counts above a threshold using the ESRF hyperspectral image processing software ARTEMIS (publicly available). The spectra from those regions were summed up to produce two final spectra from T or TP. Regions of 20 x 20 microns around the TP were also mapped at high resolution - approximately 1 x 1 micron. A separate spectrum was obtained by adding up the spectra of all pixels below threshold, containing aerogel only . These three spectra per keystone were treated using PyMCA, the ESRF spectrum analyzer software (freely available) in order to identify elements between Si and Se using their K fluorescence lines and extract their relative concentrations. All elements were detected at orders of magnitude higher concentrations with respect to the ID22 minimum detection limits (MDL). Absolute concentrations were then estimated for all detected elements using the NIST SRM 1833 thin glass standard. K, Ti, Fe and Zn present in the standard were directly used to derive absolute concentrations. All other detected elements were estimated from these four elements using fluorescence cross-sections from our XRAYLIB database *(S1)*.

High-resolution scanning SXRF measurements were performed at the ESRF Microfocus (ID13) beamline using a sub-micron hard X-ray beam of about 200 nm focus size. The pixel-size of the obtained elemental maps corresponds to a scanning step-size of 100 nm. Using an excitation energy of 13 keV, chemical elements in the atomic number range of 16-33 (S-As) could be detected based on their K-lines, while elements having atomic numbers 47-81 (Ag-Tl) could be detected based on their L emission-lines. Absolute detection limits were determined to be sub-fg in the detected elemental range, reaching 3-10 ag for elements detected with the highest sensitivity using a measuring time of 300 s. The determination of detection limits and quantitation of the measured data-sets are based on the use of MPI-DING geological glass calibration standards (described in *S2)*.

Advanced Light Source X-Ray Microprobe

The micro-SXRF and the micro-XAS Beamline 10.3.2 at the Advanced Light Source, a bending-magnet hard X-ray microprobe (described in *S3*), was used to produce SXRF maps and spot SXRF analyses, This beamline uses a Si(111) monochromator and K-B pair to deliver a focus spot ranging from 5x5 to 16x7 (HxV) microns. The detector is a Canberra UltraLeGe 7-element unit. Whole-track mapping was done at the large beam size, but only region-of-interest counts were recorded per pixel. Point spectra of individual particles were taken using a range of spot sizes. For the point spectra, backgrounds were taken at points close to but not on each particle and subtracted after normalization for deadtime and beam current.

SXRF maps were collected using incident photon energies of 10 keV and14 keV with 20 micrometer step size and a100 ms/ pixel dwell time, using a beam spot size of 7x7 micrometer.. A 7 element Ge detector positioned at 90^o. to the incident beam was used to collect the element windowed fluorescence signals. The samples were mounted on a XYZ stage positioned at 45^o. to the

incident beam. Fe and Ca-K XANES spectra were recorded on a multitude of hot spots using a Si (111) monochromator. X-ray data analysis was performed using a suite of Lab-View programs available at beamline 10.3.2. The background was subtracted, normalized and fit using a set of standards.

Advanced Photon Source and National Synchrotron Light Source X-Ray Microprobes

X-ray fluorescence (XRF) maps and spot XRF analyses were measured using the undulator-based microprobe at Sector 13 (GeoSoilEnviroCARS) at the Advanced Photon Source (APS), Argonne National Laboratory and bending-magnet based microprobe at beamline X26A at the National Synchrotron Light Source (NSLS), Brookhaven National Laboratory *(S4).* Both instruments used a Si (111) monochromator and Kirkpatrick-Baez (KB) microfocusing mirrors *(S5, S6).* The KB system consists of two mirrors (100 mm length) in tandem, one oriented horizontally and one oriented vertically. Each mirror, a highly polished, flat, single crystal of silicon coated with several hundred Å of Rh, is dynamically bent to an elliptical shape using a mechanical bender. A 300 x 300 micrometer x-ray beam incident on the mirror pair is focused by reflection to ~3x3 micrometrer (APS) and ~5x8 micrometer (NSLS). The incident beam energies were 16.5 and 23 keV (NSLS and APS, respectively). XRF spectra were collected using a Vortex-EX silicon drift detector using digital signal processing electronics with energy resolution of ~130 eV. Maps were acquired by rastering the sample in the x-ray beam with 3 and 5 μm steps for the APS and NSLS, respectively. Dwell times for maps were between 0.5-1 second and 3-17 seconds (APS and NSLS, respectively). Total mapping times were typically several hours per track. Full XRF spectra were saved at each analysis pixel. In addition, longer dwell spot XRF analyses (typically 5-16 mins) were obtained on spots along the track with high count rate (typically high Fe K count rate) in order to increase the number of detectable elements.

Spectra were processed in two ways. In some cases (C2009,20,77; C2086,1,65,0,0), all spectra in a map were summed to produce a whole-track spectrum. A portion of the map "off-track" was then summed to produce an aerogel background spectrum. The whole-track and aerogel spectra were then subtracted using total pixels summed in each for normalization. The net spectrum was then fit using a Gaussian based routine and the net peak areas converted to masses using comparable measurements on SRM thin film standards 1832/1833. NRLXRF *(S6)* was used to extrapolate sensitivities to elements not present in the SRMs.

In other cases (C115, Tracks 19-22; C2044 Tracks 7, 12 and Big Track), the long dwell time spectra on "hot-spots" were fit individually and elemental masses computed for each as above using "off-track" aerogel analyses for background subtraction. These elemental masses were then summed and scaled to produce whole-track masses. The scaling factor, required because only a fraction of the total track was analyzed, was taken to be the ratio of the Fe mass in the summed analyses and that in the map. These factors were typically in the 2-5 range but were as high as 21 in a highly dispersed track (C115 Track 19). The use of this scaling factor assumes that the average composition of the analyzed material is the same as that for all the material in the track. This assumption will be most valid for tracks produced by fine-grained aggregates and less valid for those dominated by large mineral grains.

For elements greater than Ca where self- and aerogel absorption is negligible, the precisions in the masses for the whole tracks (integrated map or sum of particle analyses) are better than 20%. There are at least 1000 counts in these integrated spectra for all elements reported corresponding to a <10% statistical uncertainty. The SRM thin film standards used for mass determinations have uncertainties of between 3 and 10%. Thus, the mass precisions are better than 20%. The error in the Fe masses are actually near 3% (counting statistics negligible, dominated by

standard uncertainty), i.e., small compared to the uncertainties in the other masses. So, the Fe normalized abundance uncertainties are about 20%.

Stanford Synchrotron Radiation Laboratory X-Ray Microprobe

The hard x-ray scanning microprobe at the Stanford Synchrotron Radiation Laboratory (SSRL), Stanford Linear Accelerator Center is an endstation of wiggler Beam Line 6-2 and has a 2 μm minimum beam size with 10^9 photons/second (photons/s). X-ray fluorescence (XRF) maps and spot analyses were performed using 14 keV x-rays from a Si (111) monochromator defined by virtual source slits and focused by Kirkpatrick-Baez optics. For whole track mapping, focused spot size was either 15x19 micrometers or 6x16 micrometers for efficient mapping with 2 to $5x10^{10}$ photons/s in the beam spot. The sample was translated in the beam in steps matched to spot size with dwell times of at least 30 seconds/pixel and as much as 500 seconds/pixel for a small track (C2044,0,39, Track 5). Full fluorescence spectra were collected at each pixel. Terminal particles and other particles along tracks were located primarily by high Fe count rate. For particle spot analyses and a few high resolution maps of terminal regions, the focused spot size was reduced to 3.5x4.5 micrometers with $3x10^9$ photons/s in the beam spot. Long count time spectra on particles were typically 2000 seconds up to 5000 seconds; however, for consistency, terminal particle data reported here were isolated from whole track maps. A Si(Li) detector with ~150 eV resolution collected the fluorescent x-rays in a geometry perpendicular to the incident beam in the plane of the storage ring. PIN diodes provided pre- and post-sample intensity measurements.

XRF map spectra were processed as follows: In mapping the track, pixels extending outside the comet particle track were also measured. The portion of the map without cometary material provided the background contribution from the aerogel. Spectra were fit using PyMca, a program developed by Dr. Armando Sole at the European Synchrotron Radiation Facility (ESRF). Whole track mass was derived from the difference between the summed track spectra containing cometary material and the averaged background concentration for the same number of pixels. Two types of reference standards were used: a thin (200 nm) Fe film was used as an absolute reference standard and a USGS basaltic glass microprobe standard (NKT-1G) was used to determine the energy-dependent correlation for elements above and below Fe. Mass precisions are generally 20% or better for elements above Ca. Statistical uncertainty is <10% for all elements reported in whole track data. For terminal particles, due to reduced total counts, the statistical error is as high as 17% in low-abundance elements, Ga and Se. Uncertainties in the thin film standard compositions are <1% for elements referenced. Error in Fe mass is dominated by uncertainty in the standard thickness and is at most a few percent.

SPring-8 X-Ray Microprobe

Tracks in four keystones were analyzed at Spring-8 by SXRF. The longest track was 3 millimeters in length. The analyses were conducted using a 15 KeV monochromatic x-ray beam. The analysis time was generally 2000 sec, but 1000 sec was used for some analyses. Data wass obtained for S, Ca, Cr, Mn, Fe, Ni, Zn, Cu, Ga, Ge, As, and Se. Abundances of other elements between S and Se could not be determined because of peak overlapping and interference from sum or escape peaks.

Entire tracks were analyzed using a broad beam up to 400x260 micrometers in size. By this analysis we obtained total XRF counts of elements in the tracks plus particles. All XRF analyses at SPring 8 were done at X-ray energy of 15 KeV. After that, the beam was narrowed down using two sets of slits and only particles were analyzed using 60x60 micron beam, in order to obtain XRF counts of elements sited in particles.

To determine a blank, all elements were collected on portions of the keystone consisting of only aerogel. Five particles of Orgueil CI chondrite with a diameter of about 150 microns were analyzed, in order to obtain XRF counts of elements with solar abundance. By averaging the five Orgueil results and normalizing to solar abundance, we obtained the elemental abundance of tracks and particles in keystones.

Conversion of XRF counts to weights of elements was done in the following procedures. For each keystone, we measured a portion of aerogel where no tracks and no particles are present. We calculated a weight of element Si in the analyzed portion was obtained from the density and the volume of the aerogel where the beam was passing through. By averaging the results of analysis of five Orgeuil standard particles and by normalizing to solar abundance, we obtained the ratio of the sensitivity of a element X to Si;

Complications in the Analysis of Particles in Aerogel

For the lightest elements we analyzed, S and, to a lesser extent Ca, a correction for the absorption of the fluorescence x-rays due to the aerogel in the path from the analyzed atom to the detector is required. The structure of the Stardust aerogel, a graduated density aerogel having very low density near the surface, about 20 mg/cc aerogel farther down, and 50 mg/cc aerogel near the bottom (optimized to produce minimal deceleration for the smallest particles, which are stopped in the upper layer, but to stop particles up to 100 microns in diameter within the 3 cm thickness) complicates this correction, since the density of the aerogel varies along the track in a manner that has not been well-characterized, and may differ from cell to cell. In addition, since some of the material extracted from tracks for examination consists of comet material distributed inside pieces of compressed or melted aerogel, sometimes large enough to significantly attenuate S fluorescence x-rays, detailed corrections for absorption have not been possible.

A second complication arises from the trace contamination of the aerogel itself. An ICPMS analysis of a cell of Stardust aerogel showed trace quantities of most stable elements were present in the aerogel. (S8)

Part of a Stardust a flight aerogel cell (C2054, 8) that was free of particle tracks was measured using an SXRM. The analyzed volume of this cell contained trace quantities of Ca (7.5 ppm), Fe (1.0 ppm), Ni (0.4 ppm), Cu (0.8 ppm), and Zn (3.1 ppm). These elements were frequently localized in hot-spots.

These contamination hot-spots complicate the background subtraction of the trace contaminants. Figure S1 shows a map of the spatial distribution of Fe and Ca in cell C2115. The Fe marks the path of the particle, while Ca is found in hot-spots throughout the aerogel. When a Ca hot-spot is coincident with the particle track, the hot-spot cannot be unambiguously identified as either contamination or comet material. Figure F shows a map obtained on a half-cell, which is 2 cm thick, thus it has many more Ca hot-spots along an analysis beam path than in a 200 to 300 μm thick keystone. But, even in the the keystones, which were analyzed to obtain the data reported in this paper, chance overlaps between contamination and the particle track will occur. Backgrounds were subtracted by analyzing comparable areas of track and adjacent, non-track aerogel, but the heterogeneous distribution of contamination in the aerogel leaves uncertainty in tbese background corrections.

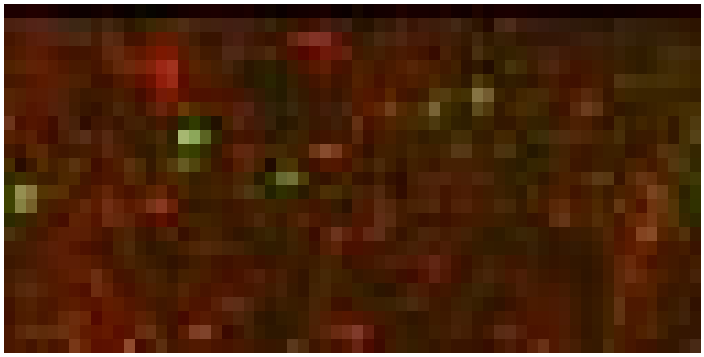

Figure S1: Map of the x-ray fluorescence intensity from Fe (green) and Ca (red) in an area centered on a particle track in Stardust aerogel cell C2115. The particle track can be identified by the Fe. This map was obtained on a half-cell of 2 cm thickness, so there are many more Ca hot-spots that we expect in a 200 to 300 micrometer thick keystone, but it illustrates the problem of correctly discriminating between a cometary Ca-rich fragment and aerogel contamination simply by its spatial association with the track.

Complex element spatial distributions in tracks are common. Track 77 is shown in an optical microscope image in Figure S2. and two false-color SXRF element maps in Figure S3 and Figure S4. Figure S3 is encoded with red proportional to the Fe concentration and blue proportional to the Ni concentration. In Figure S4, red is proportional to the Fe concentration, green is proportional to the Mn concentration, and blue is proportional to the Cr concentration. There is an obvious difference in spatial distributions of Fe and Ni in both discrete particles and the diffuse material distributed throughout the bulb of the track. It is thus necessary to integrate measurements over every part of the track. But determination of which parts of the map are in fact analyzing track material is not always unambiguous. Even among the discrete particles, there is a

Figure S2: Optical microscope image of Track 77.

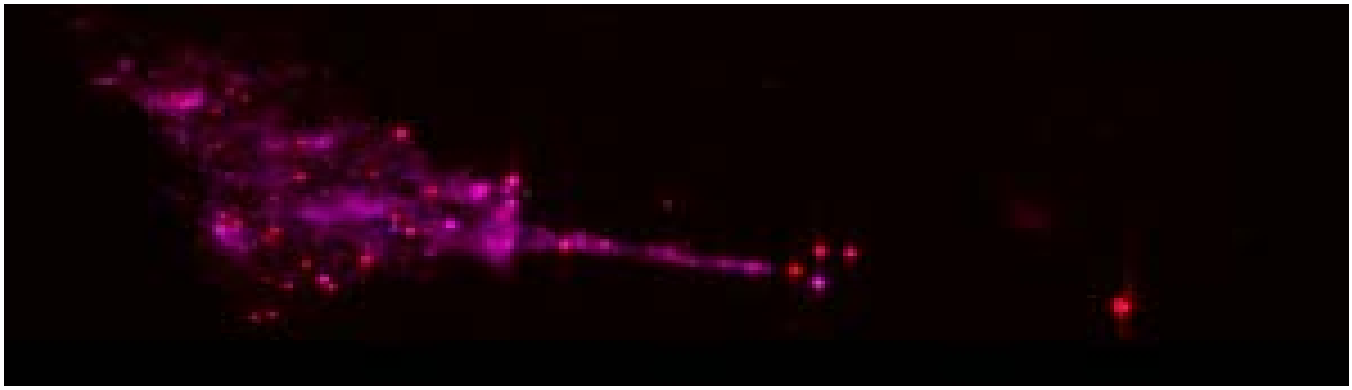

Figure S3: False-color map of the Fe (red) and Ni (blue) distribution along Track 77, showing that in many areas Ni and Fe are not colocated.

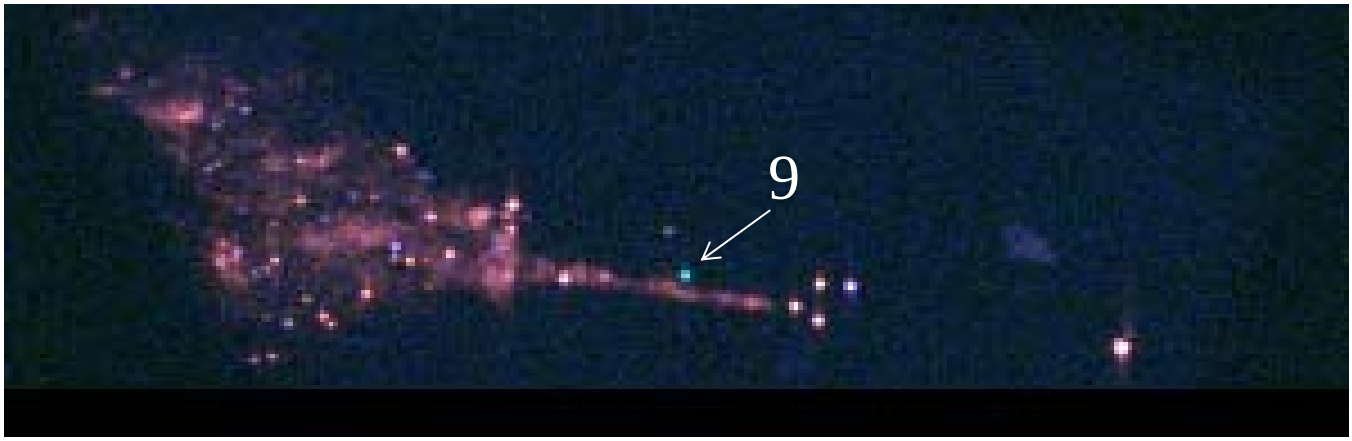

Figure S4: False-color image of the same track area in Figure S3, showing the Fe (red), Mn (green), and Cr (blue). Spot 9 is rich in Mn and Cr, but has no detectable Fe.

remarkable diversity in particle composition, and in particular in Fe content, even within this single impact. For example, the particle labelled 9 is rich in Mn and Cr, but shows no detectable Fe in this map. In the optical image of this track, 9 is the terminal particle of a track, so is unambiguously a component of the original projectile. Thus, it is critical to include spot 9 in the composition determination, but it is particularly difficult to determine its appropriate contribution to the average abundance in the hot-spot analysis technique (i.e., how many Fe hot-spots must be added to one Mn hot spot).

Statistical Uncertainty

To estimate the statistical error in the average composition of the ensemble of 23 tracks in aerogel, we assume that the observed ensemble is representative of the distribution of particle sizes and compositions of the entire dust population that was sampled by the spacecraft. We then randomly generated new ensembles of 23 tracks, by randomly drawing tracks, one at a time, from the actual ensemble. An important point is that, with the first assumption stated above, these randomly-drawn ensembles could have been seen with a probability equal to that of the ensemble

that was actually observed. We then computed the average elemental ratio for each of 10,000 such random ensembles. The distributions of the resulting elemental ratios over the 10,000 trials are in general not gaussian. We computed the 1- and 2-sigma limits in the resulting distributions by sorting the data and choosing the 1587th (228th) value from the largest and from the smallest values in the distribution. The means were computed from all measurements, assuming that the non-detections were zero. We verified that this procedure correctly reproduces the dispersion in the mean in a gaussian distribution.

A complication is accounting for non-detections -- that is, concentrations that were below detection limits. To account for these, we computed lower limits by assuming that all non-detections were identically zero. To compute upper limits, we rejected all non-detections from the ensembles -- that is, we assumed that all non-detections were identical to the detections. This is equivalent to assuming that all detections were just at the detection limit, and that all non-detections were just below the detection limit. This procedure may overestimate the upper limits, since the actual detection limits for each measurement will generally be smaller than this.

Comparison of the Hot-Spot and Track Mapping Techniques

One objective of the Preliminary Examination of the Stardust samples was to investigate a variety of techniques for analysis of particles collected using aerogel capture. Because the amount of SXRM time available for the Stardust Preliminary Examination was limited, and our first analyses demonstrated that each track was significantly different from the next one, it was necesary to devise strategies that allowed the analysis of enough tracks to obtain a convergent average composition. The limit on available SXRM analysis time precluded us from performing the analyses in the ideal mode, using a sufficient dwell time at each pixel in the map to obtain a spectrum of sufficient quality to unequivocally identify minor elements above the instrumental background. The “whole track” average compositions reported in this paper were determined using two significantly different analytical approaches. One set of tracks was analyzed by mapping the sample using relatively short dwell times per pixel, detecting only elements with $Z \geq 16$ that were present at relatively high concentrations in an analysis pixel. The element hot-spots identified by this technique were subsequently analyzed for significantly longer times, and the results from the spot analyses were summed to obtain an average composition. The longer dwell time on the hot- spots allowed the detection of trace elements that could not be seen in the maps, but this technique assumes that the composition of the hot-spots reflects the composition of material distributed more finely throughout the track volume. A second technique, in which the mapping time was increased, and the average composition was determined by adding together spectra from the area of the map provides more confidence that all of the material deposited by the particle has been included in the average, but suffers from a lower signal to noise that results from adding in many spectra that contain little elemental signal, resulting in fewer elements being detected than in the hot-spot analysis of the same track.

We compared these two basic methods to look for systematic differences. Since only one track was analyzed by different laboratories, one employing the hot-spot technique and the other the track mapping technique, the comparison is done with different particles in the data set. Figures S5 and S6 are the equivalent of Figures 2 and 3 of the text, but here the data has been separated according to the analytical method and 1-sigma error bars are shown rather than the 2-sigma error bars shown in Figures 2 and 3 of the paper. In comparing the data obtained by the spot analysis and the mapping, no systematic difference is evident between the results from the two methods. However, a systematic effect smaller than the statistical error bars cannot be ruled out by this comparison.

Further intercomparisons between the two techniques have been performed on Track 12 and Track 19.

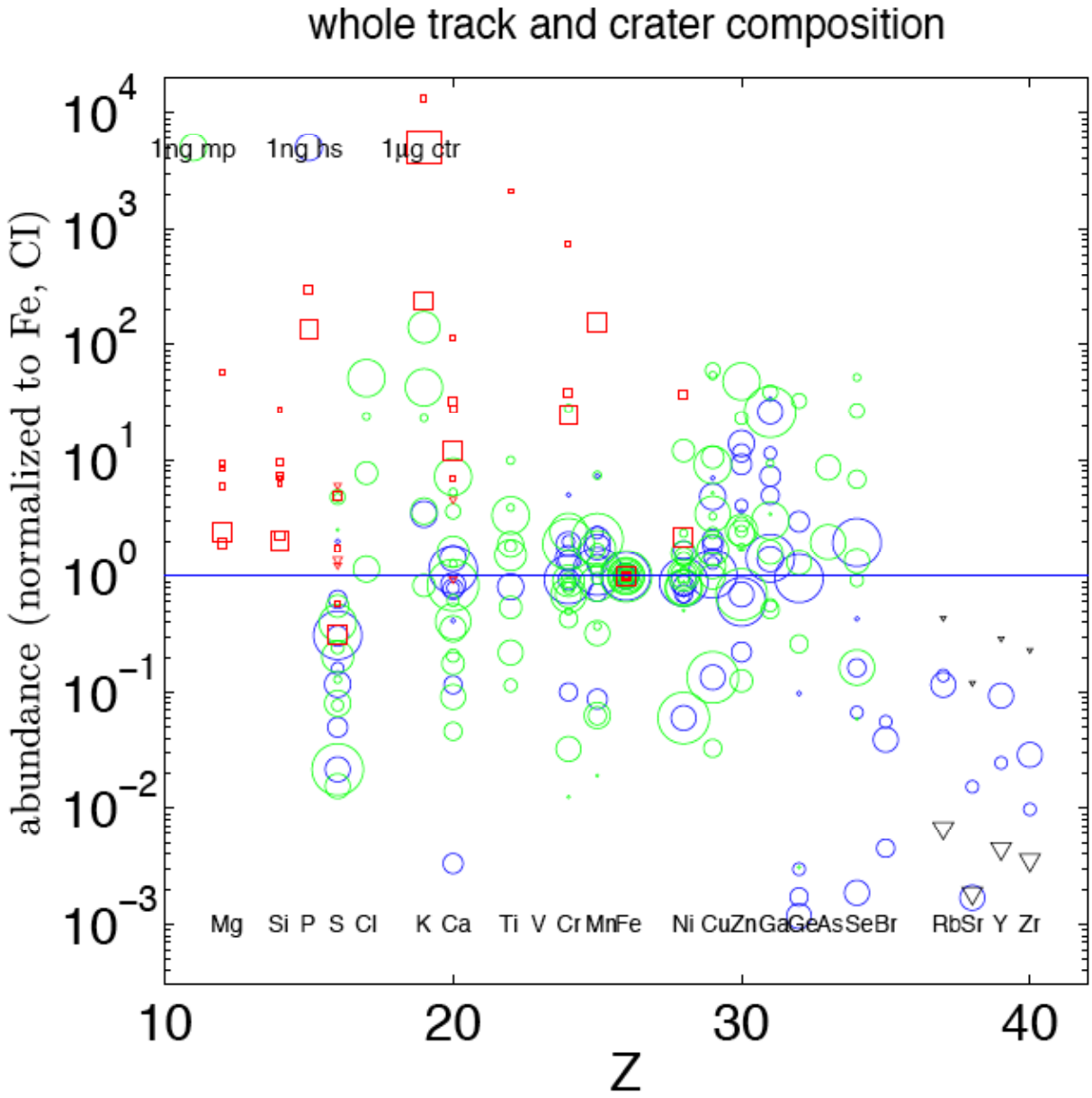

Figure S5: "Whole track" compositions of 9 tracks analyzed by the hot-spot technique (shown as blue circles) and 15 tracks analyzed by the track mapping technique (shown as green circles). One track, Tyrack 12, that was analyzed by both techniques is shown twice.

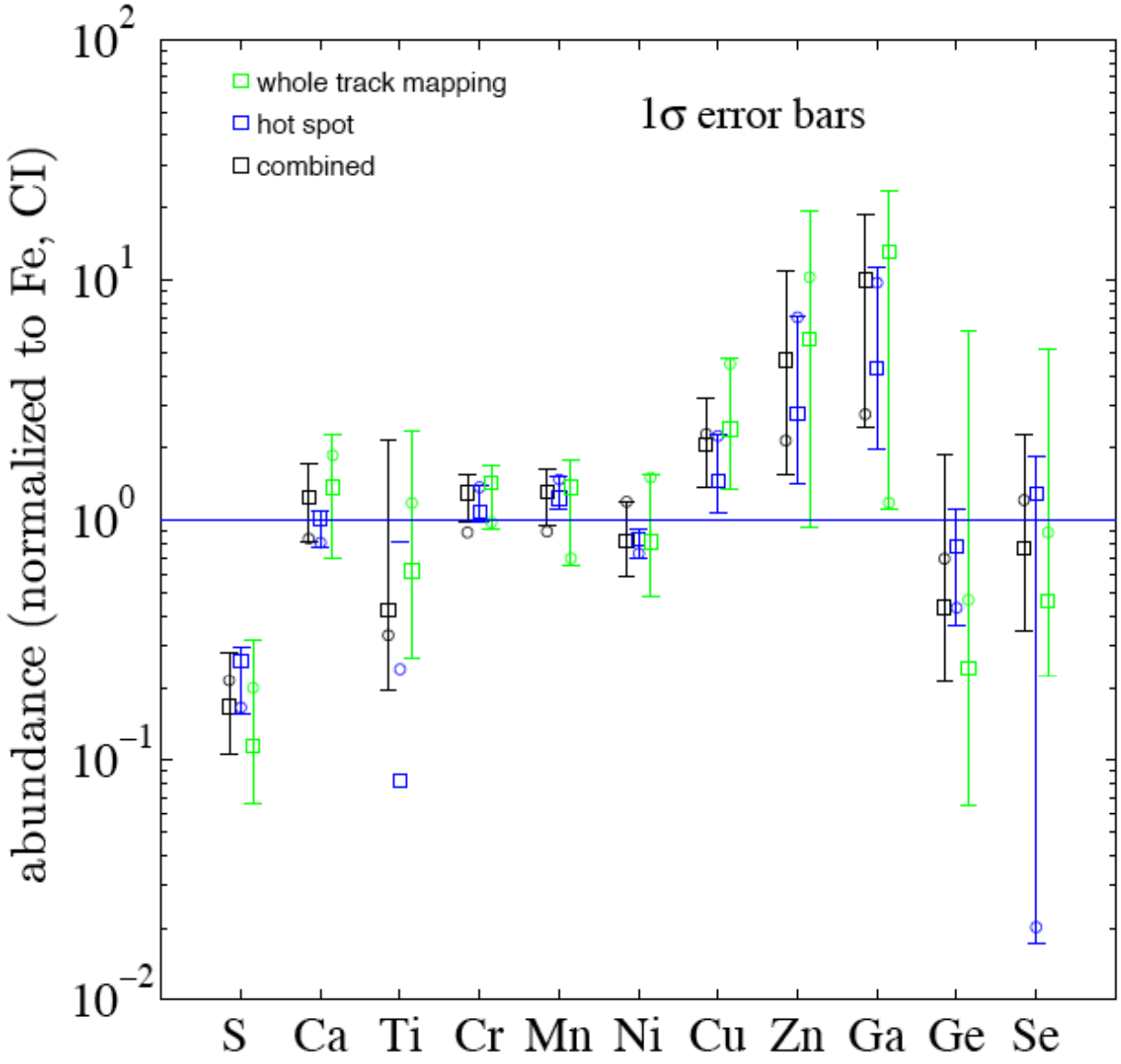

Figure S6: Comparison of the mean compositions of the 9 tracks analyzed by the hot-spot technique (shown in blue), the track mapping technique (shown in green), and the combined data (shown in black), with 1-sigma error bars generated by the Monte Carlo technique (described below) on the individual data sets.

Track 12 Analyses by Two X-ray Microprobes: Track 12 was analyzed by the NSLS and SSRL x-ray microprobes. The left plot of Figure S7 compares the Fe- and CI-normalized abundances for the elements that were detected in the terminal particle by both SXRMs. The agreement for Mn and Ni is at the 30% level and the Cr difference is 70%. The right plot in Figure S7 shows the whole track results inferred from three datasets. The "Integrated Spots (NSLS)" are the element abundances determined by summing the elemental masses for hot-spots in the track map. The "Integrated Map (NSLS)" and the "Integrated Map (SSRL)" are the element abundances determined by integrating the spectra at each pixel of each track map (upper limit indicated by arrow). All three datasets are consistent at the 40% level with the exception of Cr where there is about a factor of 3 difference between the NSLS (both methods) and the SSRL data.

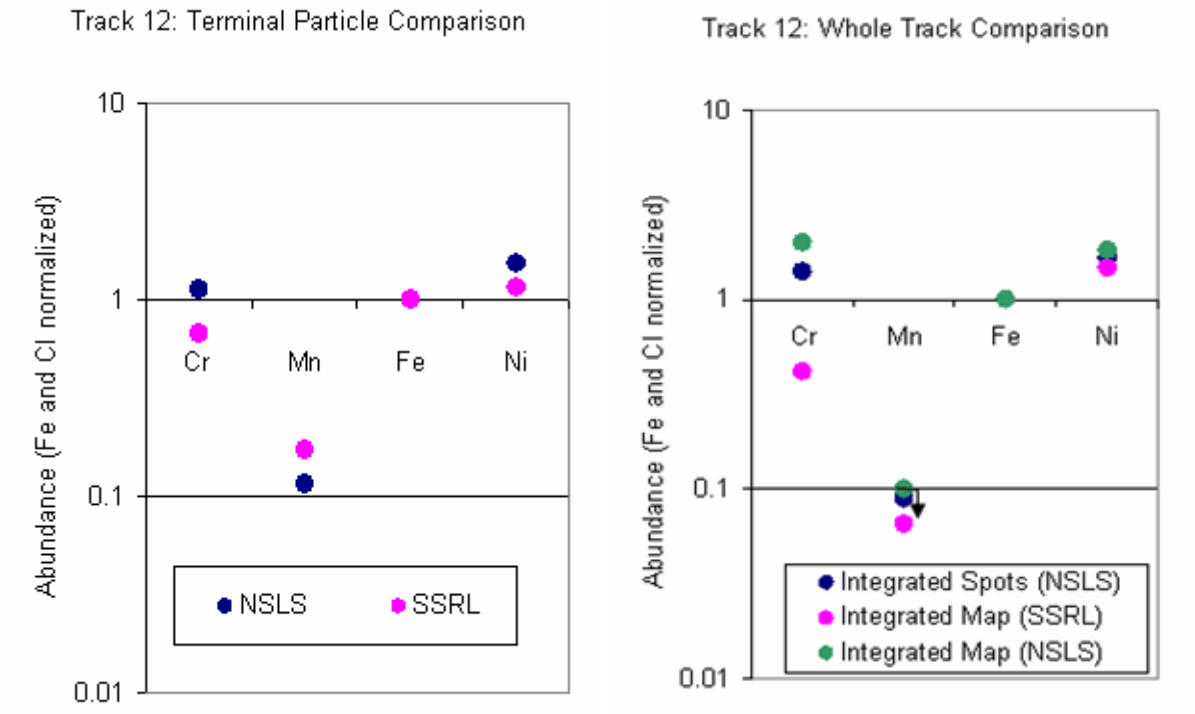

Figure S7: Comparison of the Fe-and CI-normalized elemental composition of the Track 12 terminal particle measured using the SXRF microprobes at the NSLS and SSRL (left), and the Track 12 whole track using the spot technique at the NSLS, the mapping technique at the NSLS, and the mapping technique at SSRL. In each case there is good agreement between the measurements by the different techniques.

Track 19 Analysis by Spot Integration and Map Integration: Figure S8 shows the element abundances in Track 19, analyzed at the APS, comparing the results using two different methods of "whole track" analysis: the "Integrated Spot" and "Integrated Map" methods. The results are consistent at the 25% level for Mn, Ni and Zn. Cr and Cu show differences of about a factor of two. Differences may result from the hot-spot technique analyzing a smaller fraction of the total material than the mapping method. These results together with those for Track 12 above provide evidence for the level of inaccuracies associated with integrating a subset of the track material.

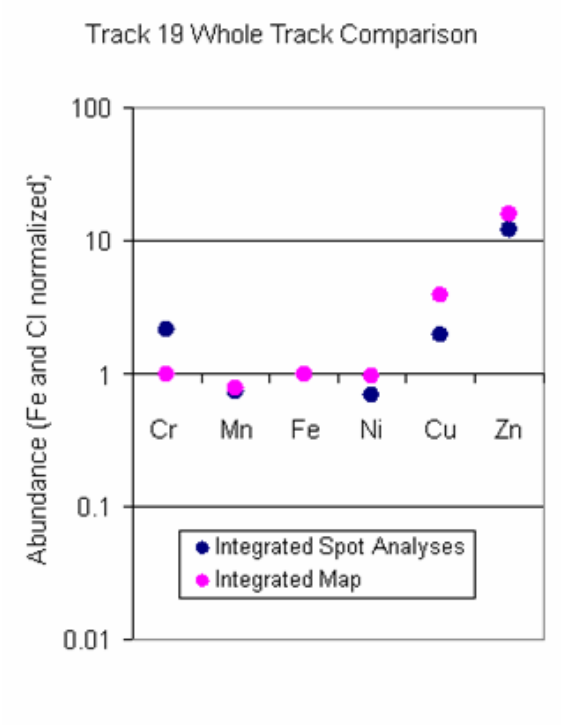

Figure S8: Comparison of the Fe-and CI-normalized elemental whole track composition of Track 19 measured using the SXRF microprobe at the APS using the spot technique and the mapping technique. There is good agreement between the measurements by the different techniques.

ToF-SIMS of Bulb Slices

Table S1 provides Fe- and CI-normalized element ratios obtained by ToF-SIMS measurements performed at the Smithsonian Institution and Münster University. Both samples are slices from one side of the bulb of track C2115,21. The track was dissected lengthwise, then one half was sectioned into many slices. Slices C2115,30,21,0 and C2115,34,21,0 were analyzed at the Smithsonian and Münster respectively. Consequently, each group analyzed only a small amount of material relative to the entire track, and each group analyzed a different part of the track. Both laboratories used identical principles of data reduction. Blank corrections were made assuming that the Si/Fe in the residue is CI-chondritic. The surplus of Si is attributed to the blank. The composition of the blanks was determined from regions in the aerogel surrounding the track. Finally, we discarded those data where the blank is higher than 50% of the entire signal or where the blank is clearly heterogeneous, and therefore a clear attribution of the measured signal to cometary material cannot be made. Data in red have high statistical error (>1/3).

Crater SEM-EDX

The chemical composition of the residue in each of the 7 large craters in the Al-foil was determined using an Oxford Instruments INCA energy dispersive X-ray (EDX) spectrometer. The analyses were performed at 20 keV and 2 nA. The exposed surfaces were rough and were not carbon coated, so the matrix corrections are approximate. These effects are described in detail by Kearsley et al. *(S10).* Wherever possible the sample was tilted to allow electron beam incidence perpendicular to the residue surface (Tilt), which permits the most appropriate matrix correction. The X-ray spectra from which the quantitative data are derived were taken from large patches of residues in the crater floor, most using the tilted orientation, with relative count rates suggesting that they are of close to micron-scale thickness. The element abundances were calculated by comparison to the suite of silicate, oxide and sulfide standards at the Natural History Museum, processed with an extended Pichou and Pouchoir (XPP) correction, then normalized to 100%,

but Al was excluded from the subsequent calculations because of the ubiquitous excitation of the Al-foil substrate. All analyses were performed in high vacuum except the analysis of C2107W,1, which was performed at low vacuum (30 Pa). All element abundances are shown in Table S2 as wt-% oxides, although S is likely to be present as a sulfide (as observed in C2029W,1).

To quantify the effect of element loss during the production of impact residue, a variety of projectiles were shot onto Stardust Al1100 foil in the light gas gun at the University of Kent at close to the Stardust encounter velocity of 6.1 km/s *(S9)*. A measure of the level of precision and comparability to pre-impact composition that can be expected for the Stardust crater residue analyses by SEM-EDX is seen in Figure S9 a plot showing the typical dispersion

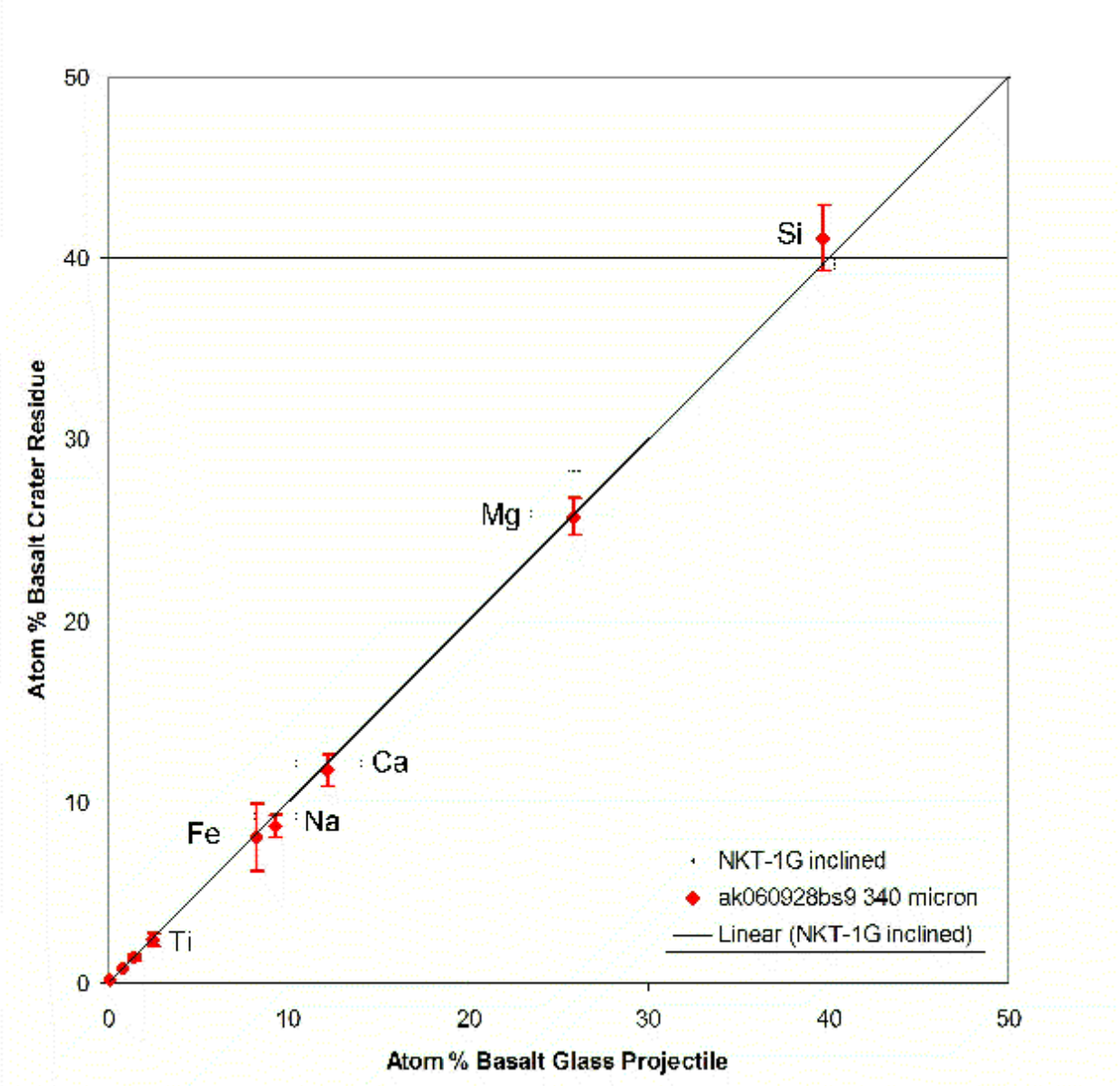

Figure S9: Comparison of the composition of the basaltic glass composition with the results of SEM-EDX analyses of the residue analyzed in craters produced by shooting the glass, at ~6 km/sec, into Stardust Al1100 foil.
(grey error bars) of analyses expressed as atomic ratios in a comparison between light gas gun residues of basalt impact and a suite of rough projectile surfaces (of known composition).

Experiments with pyrrhotite (Fe-sulfide) projectiles demonstrated that there is loss of sulfur during impact. SEM-EDX analyses of residue on the rough floor of craters of less than 10 micrometers diameter gave poor data due to substantial matrix correction problems, but analytical transmission electron microscopy (AEM) at Lawrence Livermore National Laboratory on a focused ion beam section through a 12 micrometer diameter crater showed reduction in sulfur from 39% to 27% by weight in the residue. SEM-EDX of residue in craters of 150-200 microns diameter showed depletion from an original sulfur content of 39% by weight in the projectile, to 33% in the residue. Larger craters, >300 micrometers in diameter, contain coarse patches of residue (several micrometers thick) that are indistinguishable from the projectile in composition, although S is lost from thinner residues in the same crater.

Analytical Electron Microscope data from sub-micron thickness basalt residue layers in small laboratory impact craters, <20 micrometers in diameter, are shown in Figure S10. Localized depletion of Na (0-28% loss), Mg (0-9% loss), Si (10-14% loss) and Fe (0-10% loss), were observed, although almost all the AEM spectra have essentially the same composition as in the projectile, except for some loss of Si *(S9).* There is little change in any of these elements in craters >50 micrometers in diameter, except very minor Na loss (see Figure S9).

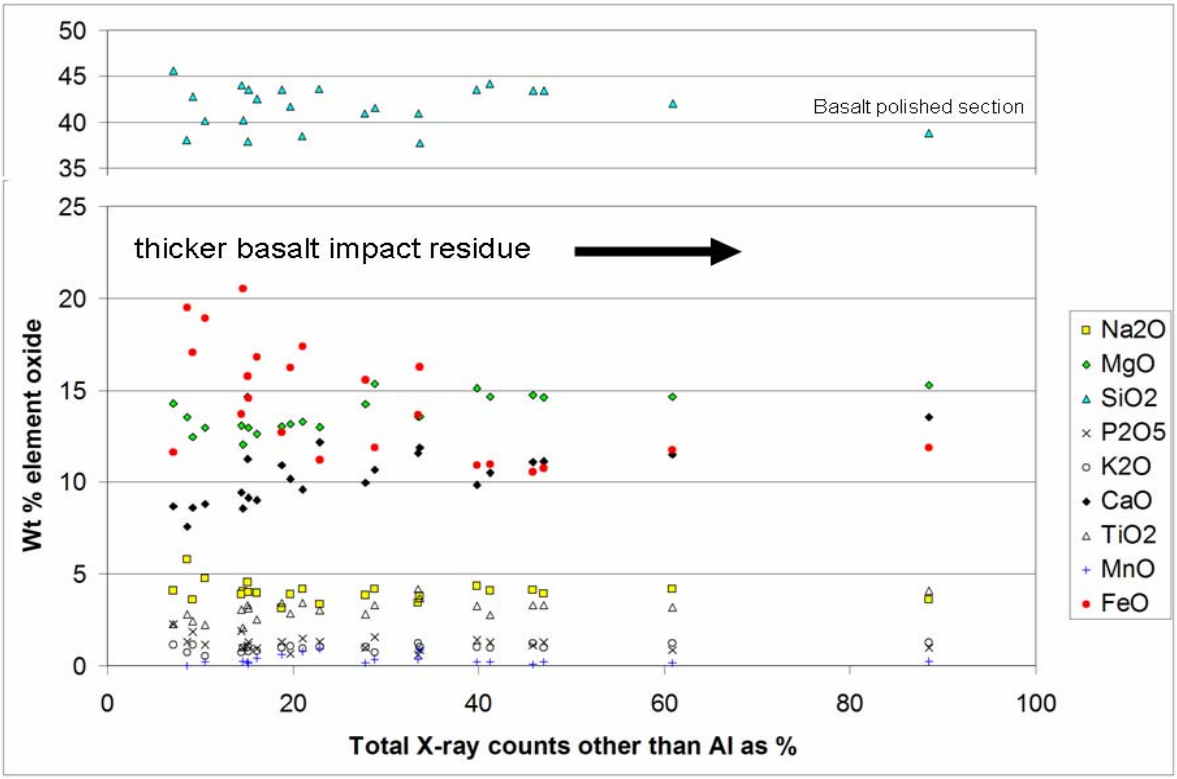

Figure S10: Weight-% oxide analyses of residue in small craters (<20 micrometer diameter) produced by shooting basalt projectiles into Al1100 foil shown as a function of residue thickness indicate that the analyses are quite variable in the very thin residues of the smalllest craters, but quickly converge as residue thickness increases.

Figure S10 shows SEM-EDX wt %-oxide data from individual analyses of basalt residue (normalised and without Al_2O_3) plotted against a horizontal axis in which the % figure reflects the proportion of residue (as opposed to Al substrate) in the determination. The close match between crater data and the polished section analysis (89%, near right) suggests that there is no

substantial problem due to either loss during impact or due to the analysis technique, although there is clearly dispersion of the Fe and Si figures in the thinner residues with lower residue wt%, probably due to a contribution from X-rays generated in inclusions within the underlying alloy. This implies that there is no substantial underestimation of the alkalis in the large crater EDS data, and certainly not so large as the apparent discrepancy between EDS and ToF-SIMS data might suggest. The spot EDX analyses all used a 50-second X-ray collection from a tightly focussed spot at 2nA current and 20kV accelerating voltage, which is a relatively gentle irradiation compared to conditions for wavelength dispersive X-ray analysis (ten times higher beam current and perhaps three times as long for acquisition), where it has been established that alkali migration does occur. X-ray maps which gave very short beam irradiation, less than 0.1 second per micron total, showed high alkali contents in two craters, but also that the alkalis were not distributed evenly at the micron scale. In these craters analyses were taken from scanned areas, with much lower beam irradiation than spot analyses.

TOF-SMS Analysis of Craters

The residues in 5 craters were analyzed by Time-of-Flight Secodary Ion Mass Spectroscopy (ToF-SIMS), using procedures described by Hoppe et al. *(S11)* and element sensitivities described in Stephan *(S12)*. Earlier investigations *(S11)* have shown that ToF-SIMS analysis of the residual matter in hypervelocity impact craters, the projectile material can be identified and its composition can be determined. In the TOF-SIMS instrument, the primary ion beam reaches the sample at an angle of 45°. For samples with high topography, like impact craters, different regions are reached by the ion beam under different orientations, so different areas are analyzed when the sample is rotated. Consequently, the observed differences in the results from impact craters analyzed in two different orientations indicates there is a heterogeneous distribution of the elements in these crater.

To verify the ToF-SIMS analyses of impact residue, four projectiles of mineral standards, bytownite, diopside, hornblende, and olivine, were shot into Al-foil using light gas guns at the University of Kent and the NASA Johnson Space Center at close to the Stardust encounter velocity of 6.1 km/s. Figure S11 compares the ToF-SIMS analyses of residues in impact craters with SEM-EDX analysis of these standards. The results show that the ToF-SIMS analyses are generally in very good agreement with the SEM-EDX results. Error bars for TOF-SIMS data show the variation range for measurements that have been performed on three different craters for each mineral. In case of hornblende and especially diopside, an apparent enrichment for TOF-SIMS Na data was observed. In both cases, this can be attributed to Na contamination of the foil, since an alkali contamination is distributed in these foils rather heterogeneously (a lot of alkali hotspots were found outside the craters). Therefore, blank correction is very difficult here, and only an "average blank" was subtracted. Similar observations were also made for some craters in Stardust foils.

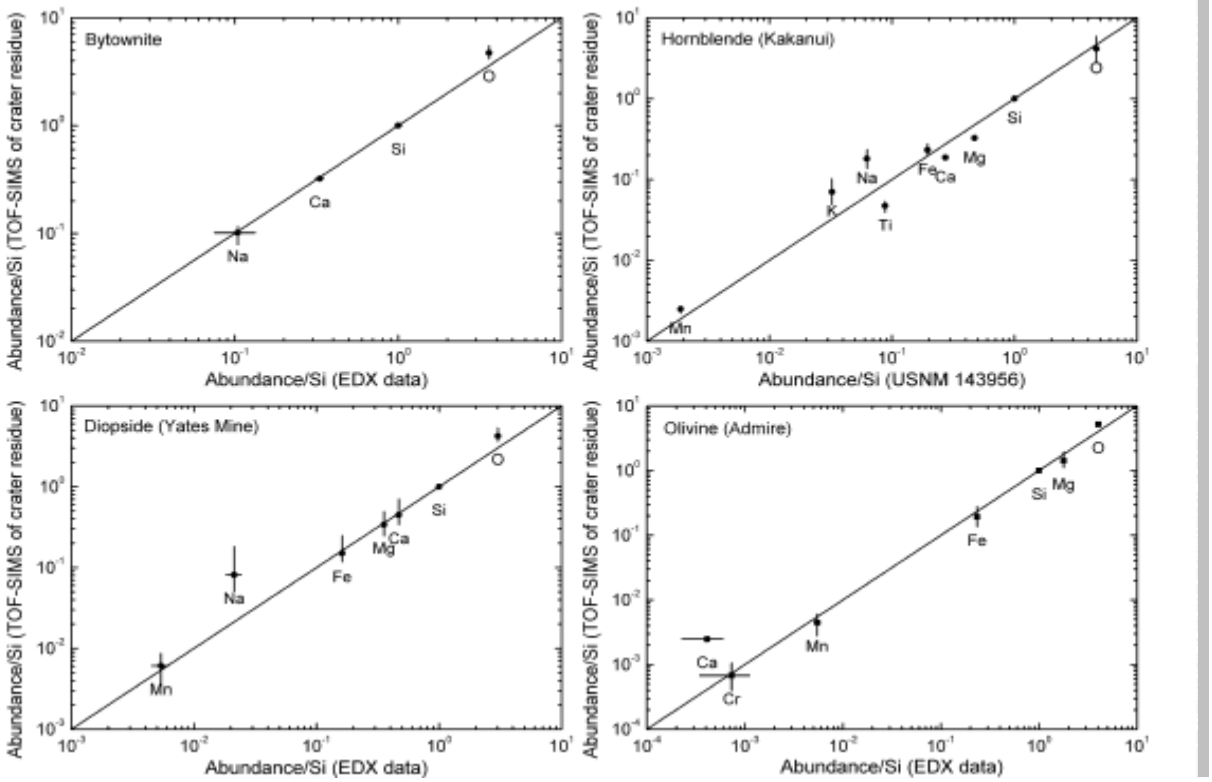

Figure S11: Comparison of the compositions of four mineral standards determined by SEM-EDX with the compositions determined by ToF-SIMS analyses of residues in craters produced by shooting these standards into Al-foils.

References

S1 A. Brunetti, M. Sanchez del Rio, B. Golosio, A. Simionovici, A. Somogyi, A Library for X-Ray-matter Interaction Cross Sections for X-ray Fluorescence Applications, *Spectrochim. Acta B* **59**, 1725-1731, 2004.

S2 New geological standard reference glasses for in situ microanalysis, K.P.Jochum, D.B. Dingwell, A.W. Hoffmann, B. Stoll, I. Raczek, A Rocholl, S. Becker, A. Besmehn, D. Besette, H.J. Dietze, P. Dulski, J. Erzinger, E. Hellebrand, P. Hoppe, I. Horn, K. Janssens, G. Jenner, M. Klein, W.M. McDonough, M. Maetz, I.K. Nikogosian, C. Pickhardt, H.M. Seufert, S.G. Simakin, A.V. Sobolev, B. Spettel, S. Straub, L. Vincze, A. Wallianos, G. Weckwerth, D. Wolf and M. Zimmer, *Geostandards Newsletter*, **24:** 87-133 (2000).

S3 M. A. Marcus, A. A. MacDowell, R. Celestre, A. Manceau,T. Miller,H. A., Padmore, and R. E. Sublett, Beamline 10.3.2 at ALS: a hard X-ray microprobe for environmental and materials sciences", *J. Synchrotron Radiation*, **11**, 239-247 (2004):

S4 S. R. Sutton, P. M. Bertsch, M. Newville, M. Rivers, A. Lanzirotti and P. Eng, Microfluorescence and microtomography analyses of heterogeneous earth and environmental materials, Re-

views in Mineralogy & Geochemistry: Applications of Synchrotron Radiation in Low-Temperature & Environmental Science, *Mineralogical Society of America*, **49**, 429-483 (2002).

S5 P. Kirkpatrick P. and A. V. Baez, Formation of optical images by X-rays. *J Opt Soc Am* **38**:766 (1948).

S6 P. J. Eng, M. Newville, M. L. Rivers, and S. R. Sutton, Dynamically figured Kirkpatrick-Baez micro-focusing optics. In "X-Ray Microfocusing: Applications and Technique" (ed. I. McNulty), *SPIE Proc. 3449*, 145 (1998).

S7 J. W. Criss, L. S. Birks and J. V. Gilfrich, Versatile X-ray analysis program combining fundamental parameters and empirical corrections. *Anal Chem* **50**:33-37 (1978).

S8 P. Tsou et al., *J. Geophy. Research*. **109**, Issue E12, E12S01 (2004).

S9 A. T. Kearsley, M. J. Burchell, P. Wozniakiewicz, M. J. Cole, G. A. Graham, R. J. Chater, Z. Dai, N. Teslich, F. Horz and C. Schwandt, *Meteoritics & Planetary Science, in press*..

S10 A. T. Kearsley, M. J. Burchell, F. Hörz, M. J. Cole, and C. S. Schwandt, *Meteoritics and Planetary Science* **41**, 167-180 (2006).

S11 P. Hoppe, F. J. Stadermann, T. Stephan T., C. Floss, J.Leitner, K. K. Marhas and F. Hörz SIMS studies of Allende projectiles fired into Stardust-type aluminum foils at 6 km/sec. *Meteoritics & Planetary Science* **41**, 197–209 (2006).

S12 T. Stephan TOF-SIMS in cosmochemistry. *Planet. Space Sci*. **49**, 859–906 (2001).

Table S1: TOF-SIMS examination of residual cometary matter found in two aerogel slices cut perpendicular to track 21 in cell C2115. Given are Fe- and Ci-normalized concentrations after aerogel blank corrections. Errors are 1σ, based on counting statistics.

	C2115,30,21,0 (Smithsonian)		C2115,34,21,0 (Münster)	
	Fe- and CI-normalized	error	Fe- and CI-normalized	error
Na			1.25	0.06
Mg	0.870	0.017	0.525	0.011
Al	1.28	0.07	0.69	0.04
Ca	0.19	0.03	0.202	0.022
Ti	1.6	0.7		
Cr	0.96	0.20	0.85	0.17
Mn	1.0	0.3	0.9	0.5
Fe	1.00	0.04	1.00	0.03
Co	1.1	0.9	1.9	1.1
Ni	3.5	0.4	2.6	0.4

Table S2: Bulk residue composition in Stardust foil craters of greater than 50 microns diameter. All analyses are averages or area integrals, performed using an Oxford Instruments INCA energy dispersive X-ray spectrometer using 20kV and 2nA. Surfaces were rough and with no carbon coat, matrix corrections are therefore approximate. Aluminium was excluded from the fitting routine due to ubiquitous excitation of the metal substrate (not determined = nd), and results were normalised to 100%. Wherever possible the sample was tilted to allow electron beam incidence perpendicular to the residue surface (Tilt), giving best matrix corrections. All analyses at high vacuum except C2107W,1 (low vacuum LV, 30 Pa). All determinations are shown as wt% oxides, although S is likely to be as sulphide, as observed in C2029W,1. Determinations of less than 3 times background variation are shown as "<." If detected in more than one determination for the crater, the element is listed as 'trace'. The ratio of the sum of the divalent cations (minus iron for FeS) to Silicon is shown as '[Div]/Si'. Mg: (Fe-S) ratio is intended to show ratio in silicate, with Fe subtracted for inclusion in FeS. Probable mineralogy is based upon evidence of stoichiometric relations typical of a particular mineral family: 'Ol' is olivine; 'Px' pyroxene; 'Su' sulphide; 'non-stoich' residue may be 'mafic' (Ma) and/or 'alkaline' (Ak) rich. The K detection limits are 0.1 or 0.2 in all samples except C2086W,1 where the limit is 0.6.

Crater	C2009N,1	C2029W,1	C2086W,1	C2086N,1	C2091N,1	C2107W,1	C2118N,1
Morphology	Bowl	Field	Bowl?	Bowl	Field?	Bowl	Bowl
Diameter (microns)	64	167 x 133 irregular	238	57	62	85	68
Method	Normal EDS	Normal EDS	Tilt EDS	Tilt EDS	Normal EDS	Tilt EDS LV	Tilt EDS
Oxide wt %	Point analyses	Whole area integrated	Small area integrated	Point analyses	Point analyses	Point analyses	Point analyses
SiO_2	47.4	26.0	35.7	41.5	46.6	49.0	54.3
TiO_2	<	0.1	<	<	<		<
Al_2O_3	nd	nd	Nd	nd	nd	nd	nd
MgO	38.0	33.4	26.9	55.4	40.2	38.3	21.4
Cr_2O_3	3.1	0.2	0.2	0.5	trace	trace	1.2
MnO	<	0.4	0.5	<	<	trace	trace
FeO	10.6	20.1	31.5	2.7	13.2	11.8	10.1
NiO	<	2.4	0.2	<	<	<	<
Na_2O	<	0.2	2.0	<	<	<	6.1
K_2O	<	<	trace	<	<	<	1.1
CaO	<	1.1	1.0	<	<	0.9	3.1
P_2O_5	<	<	0.2	<	<	<	0.3
SO_3	0.7	16.1	1.6	<	<	trace	3.0
Comment	7 points, Cr variable from below detection.	Much Fe and S as Sulfide , Al with Na in Px?	2 mixed phases. K_2O reaches 0.6 wt%.	12 points across crater floor	5 points on crater top lip.	10 points on crater floor. Also trace Cl.	Also trace Cl
[Div]/Si	1.5	1.0 (Px)	2.0 (Ol)	2.0 (Ol)	1.6	1.4	0.8
Mg:(Fe-S)	6.5	35.8 (Px)	2.1 (Ol)	36.5 (Ol)	6.4	5.8	5.2
Probable mineralogy	Unknown	Px, Su, and non-stoich Ma	Ol (Fo 65) + non-stoich Ak	Ol (Fo 97)	Unknown	Unknown	Non-stoich Ma/Ak
Estimated mass (ng)	3.4	17	178	3.1	3.1	8.0	4.2

Table S3: SXRM analyses of Stardust tracks in aerogel keystones

		S	Ca	Cr	Mn	Fe	Ni	**Cu**	**Zn**	**Ga**
C115 Tr19	Whole Track	47468	1483	373	1950	257912	10595	270	5150	67
C115 Tr20	Whole Track	2347	81	288	305	3967	159	20	25	7
C115 Tr21	Whole Track	4369	3639	2685	2349	93103	3605	86	662	56
C115 Tr22	Whole Track	4500	29385	19364	15632	709305	2477	68.00	856.00	970.00
C2044 Tr 12 NSLS	Whole Track	5248	59	7147	2282	360143	34979	482	139	
C2044 Track 36 "BIG	Whole Track	25668	52926	15318	14010	748932	38322	2598	18114	55
C2009,20,77	Whole Track	441862	274693	65480	56916	4892327	253626	3644	5098	366
C2086,1,65,0,0	Whole Track	32789	14048	4920	4856	368203	17536	549	5872	140
C2027	Whole Track	153000	475000	46400	24000	1330000	61300	8630	111000	211
C009_04APR06	Whole Track	634	1070	121	65.6	16900	1100	39.9	52.8	8.3
C009Tr2 24MAR	Whole Track	60100	82500	13300		1020000	60500	1230	4450	
C2009_27MAR06	Whole Track	51600	2810			321000	225000	2440	70	
C2009_29MAR06	Whole Track	18768	13942	7929	529	800742	47121	706	3294	
C009_03APR06	Whole Track	1832	2480	921	816	81496	4440	139	349	
Track 32	Whole Track	1070		0.26	0.29	1440	42.4	5.4	4.3	0.26
Track 68	Whole Track	93800	12000	880	1170	66600	5380	2850	327	135
Track 67	Whole Track					180	9.5			
Track 47	Whole Track					1260				
C2044,0,38 (Track 4)	Whole Track	3389	3353	347	2524	744615	69123	526	*43*	63
C2044,0,39 (Track 5)	Whole Track	11640	2200	3376	653	8372	1156	322	*4*	*1*
C2044 Track 9	Whole Track	7285	1047	1224	1208	102327	5958	*9*	4071	3
C2044,0,43 (Track 10	Whole Track	*537*	43033	20996	19235	2134406	99773	5292	*12*	*3*
C2044 Tr 12 SSRL	Whole Track	*5208*	456	1832	196	298381	25940	43	*56*	14

Table S4: Time-of-Flight Secondary Ion Mass Spectrometry Analysis of 5 Craters in Stardust Al-foil

	C2009N,1		C2029W,1				C2086W,1				C2086N,1		C2091N,1	
est. mass [ng]	3.4		17				178				3.1		3.1	
			0°		180°		0°		180°					
	Si and CI normalized		Si and CI normalized		Si and CI normalized		Si and CI normalized		Si and CI normalized		Si and CI normalized		Si and CI normalized	
Element	Ratio	Error	Ratio	Error	Ratio	Error	Ratio	Error	Ratio	Error	Ratio	Error	Ratio	Error
Li	2.9	0.4	65	9	13	3			2.0	0.8	0.5	0.3	2.4	0.5
Na	1.487	0.007	174.8	0.3	24.39	0.09	7.94	0.03	22.23	0.06	0.615	0.007	8.07	0.02
Mg	0.775	0.002	22.89	0.05	4.031	0.015	0.368	0.002	0.493	0.004	1.123	0.003	0.999	0.003
Si	1.000	0.010	1.00	0.07	1.00	0.04	1.000	0.016	1.000	0.015	1.000	0.016	1.000	0.011
K	2.75	0.03	159.3	1.0	12.7	0.2			4.70	0.10	0.94	0.03		
Ca			27.91	0.17	3.52	0.05	0.741	0.012	0.734	0.014				
Sc			23	11	12	5	1.2	0.8			0.7	0.6	2.6	0.9
Ti	0.44	0.05							1.10	0.18	0.45	0.09		
Cr	0.56	0.02							0.09	0.02	0.53	0.02	0.45	0.03
Mn	0.50	0.02	0.86	0.18	0.55	0.09	1.59	0.07	0.61	0.06	0.148	0.018		
Fe	0.270	0.010	1.00	0.03	0.270	0.009	0.432	0.005	0.573	0.007	0.0354	0.0015	0.285	0.018
Co	0.24	0.05	4.0	1.0	6.5	0.9							0.14	0.06
Ni	2.30	0.06	4.0	0.3	1.03	0.11	0.27	0.06	0.17	0.07			0.21	0.03